Load Observing System Based on Wave Reflection for Soft-Switching Control of MHz-Frequency Resonant Inverter Against Load Fluctuations

Oyane, Aoi
Graduate School of Frontier Sciences, The University of Tokyo

Umetani, Kazuhiro
Graduate School of Natural Science and Technology, Okayama University

Hiraki, Eiji
Graduate School of Natural Science and Technology, Okayama University

https://hdl.handle.net/2324/7437047

出版情報：IEEE Access. 13, pp.127126-127141, 2025-07-10. Institute of Electrical and Electronics Engineers (IEEE)
バージョン：

Date of publication xxxx 00, 0000, date of current version xxxx 00, 0000.

Digital Object Identifier 10.1109/ACCESS.2024.Doi Number

Load Observing System Based on Wave Reflection for Soft-Switching Control of MHz-Frequency Resonant Inverter Against Load Fluctuations

Aoi Oyane[1], Kazuhiro Umetani[2], (Member, IEEE), and Eiji Hiraki[2], (Member, IEEE)

[1]The Graduate School of Frontier Sciences, The University of Tokyo, Chiba 277-8561, Japan

[2]The Graduate School of Natural Science and Technology, Okayama University, Okayama 700-8530, Japan

Corresponding author: Aoi Oyane (oyane.aoi@edu.k.u-tokyo.ac.jp).

ABSTRACT Applying MHz-frequency inverters to radio frequency (RF) power sources for plasma applications has been challenging because capacitive loads caused by load fluctuations cause destructive hard-switching. This paper proposes a MHz-frequency load impedance estimation method for soft-switching control. The proposed system estimates the load impedance by utilizing a directional coupler that is typically built into an RF power source to observe traveling and reflected waves. Therefore, unlike typical low-frequency power electronics systems, the proposed system does not require output current sensors which are not suitable for MHz-frequencies. In the experiment, the proposed method was tested using the auxiliary switch-inductor circuit of a 3.75MHz gallium nitride (GaN) full-bridge inverter as the control target. Capacitive load detection by the proposed method was experimentally verified, and soft-switching control was realized under capacitive load. The transient response of the control under a fluctuating load that changes from inductive to capacitive was also measured. The inverter transitioned to soft-switching within 2.31μs after a load change, and hard-switching took only 8 cycles.

INDEX TERMS capacitive load, load fluctuation, reflected wave, directional coupler, MHz-frequency, resonant inverter, soft-switching, switched-inductor, GaN-HEMT

I. INTRODUCTION

High frequency power supplies have been used to generate plasma [1]–[6]. These days, RF power sources are essential for a variety of technologies, including plasma processing in semiconductor device manufacturing and high frequency wireless power transfer (WPT) systems. Originally, RF linear power amplifiers were used as RF power supplies for such applications [7]–[9].

In recent years, with the improvement of the high-speed switching capability of power transistors, high-efficiency switching-mode resonant inverters have become widely used in a variety of applications [10]–[14], such as class-D, class-E, and class-Φ2 inverters. These inverters are replacing less efficient traditional linear power amplifiers in the applications of WPT, low kHz-frequency high power plasma, and MHz-frequency very low power plasma. In these kinds of inverters, power losses can be significantly reduced by operating in soft-switching mode.

Nonetheless, the use of inverters has not yet progressed much in MHz-frequency high-power plasma applications. The first problem is the vulnerability of inverters to load fluctuations caused by the nature of plasma [1], [2], [4], [15], [16]. Generally, low-loss soft-switching operation is only possible under inductive load conditions that cause lagging-phase currents. Under capacitive load conditions, leading-phase currents cause high-loss hard-switching, leading to thermal destruction of the switches.

The second problem is the difficulty of estimating the load impedance at MHz-frequencies. As one of the few solutions to overcome the first problem, a soft-switching control technique has been proposed in previous studies [17], [18], which involves canceling the leading-phase current by manipulating an auxiliary switched-inductor inserted in parallel with the inverter. This technique requires detection of capacitive load and phase-shift control of the switched-inductor according to the estimated load impedance. However, previous studies [17], [18] have not considered sensing components and load estimation methods, and the control technique was not yet complete as a practical system. Accurate load estimation at MHz-frequency is difficult because typical current sensors, which are essential for estimating the load condition [19], [20], only guarantee measurement accuracy up to the kHz-frequency range. At MHz-frequencies, significant distortions occur in the measured phase angle and amplitude of the current, increasing the measurement errors between the current and voltage sensors. Although several challenging attempts have been made to observe current in the MHz range [16], [21], they generally require precise tuning and calibration, which increases cost.

In this paper, the proposed method utilizes a directional coupler as an observer instead of voltage and current sensors. Directional couplers are commonly used to measure RF traveling and reflected waves at MHz [22] and GHz frequencies. Directional couplers have traditionally been built into linear RF power supplies to monitor traveling and reflected powers [23], and future switching RF power supplies using MHz inverters will certainly also include directional couplers for the same purpose.

In the proposed system, the directional coupler is repurposed for capacitive load detection and load impedance estimation for soft-switching control, eliminating the need for a current sensor and thus avoiding the second problem mentioned above at MHz-frequencies. The parameters used for load estimation are the reflection coefficient and reflection phase angle, which can be obtained from the traveling and reflected waves monitored at the directional coupler. These waves are waves of energy that propagate on the RF output power line (transmission cable). The traveling wave propagates from the inverter (RF source) to the load, and the reflected wave returns from the load to the inverter due to reflection at the load.

Load estimation using the proposed method makes the soft-switching control technique feasible as an inverter system. Therefore, the first problem is also solved, and MHz inverters become applicable to load-varying systems.

In this study, the prototype inverter to demonstrate the control is composed of a full-bridge switch, with an auxiliary switched-inductor. The switching frequency is 3.75MHz, and all the switches used are gallium nitride high electron mobility transistors (GaN-HEMT). The controller is programmed to not operate the switched-inductor if inductive load is detected since no control is required. Only when capacitive load is detected, does the system perform phase-shift control of the switched-inductor according to the estimated load value. This control cancels the leading-phase current of the full-bridge switch due to capacitive load, allowing operation in soft-switching mode.

In the experiment, the detection of capacitive load was confirmed by the lighting up of an LED in the control circuit. The operation mode of the inverter was checked using an oscilloscope.

As a result of the experiment, when the load was set to inductive, the LED did not light up, the switched-inductor did not operate, but the inverter was in soft-switching operation. In contrast, when the load was set to capacitive, the LED lit up, the switched-inductor operated, and the inverter performed soft-switching operation. To summarize these results, the proposed system distinguished between inductive and capacitive loads and realized soft-switching control under the capacitive load as intended.

The transient response of the system was also tested when the load was changed from inductive to capacitive. As a result, the inverter operation transitioned from hard-switching to soft-switching within 2.31μs immediately after the load changed. During this transition, only 8 cycles of hard-switching occurred.

This study is an interdisciplinary effort. Directional couplers and reflection theory have traditionally been used in RF electronics and microwave engineering, while full-bridge inverters, switched-inductors, and phase-shift operation have been used in kHz-frequency power electronics. Therefore, the proposed system is a hybrid of RF methodology and power electronics, realizing the control of a modern MHz inverter.

This paper is a further development based on the author's conference presentation [24]. New detailed experiments were conducted using the reconstructed prototype.

This paper is divided into eight sections. Section 2 discusses the difficulties of applying inverters in applications with capacitive loads. Section 3 provides an overview of the proposed load estimation method for inverter control. Section 4 explains the principle of the load estimation based on the traveling and reflected waves. Section 5 describes the circuit configurations and operating principles of the experimental prototype of the proposed observer. Section 6 describes the prototype inverter system to test the soft-switching control. Section 7 shows the experimental results. Section 8 is the conclusion.

II. PROBLEMS DUE TO CAPACITIVE LOAD

A. DIFFICULTIES IN REPLACING LINEAR AMPLIFIERS WITH INVERTERS

The use and control of MHz-frequency inverters for high-power plasma applications have not been widely studied [1]–[4], [25]. This is because many of RF power sources used in today's high-power plasma systems are still based on traditional linear power amplifiers [7]–[9].

Linear amplifiers have low efficiency, but are robust to load fluctuations, making them suitable for plasma applications. A linear amplifier produces a sinusoidal RF output by changing the resistance of power transistors in a sinusoidal or half-sinusoidal manner. Due to its high resistance, the power conversion efficiency of the linear amplifier is less than about 70-80% even under optimum load. Therefore, a linear amplifier always generates considerable heat and must be equipped with a large heatsink. Load fluctuation is not a serious problem because this heatsink has sufficient heat dissipation capability to handle additional heat due to load fluctuations.

On the other hand, switch-mode inverters have the advantages of high efficiency around 90% and low heat generation at the optimum load due to soft-switching, but the allowable load variation range is narrowly limited to inductive loads. Capacitive load conditions cause hard-switching in the inverter. Since the switching cycle is short in the MHz range, the transistors generate significant heat due to switching losses under hard-switching conditions. One of the motivations for using switch-mode inverters is to downsize the heatsink. However, small heatsinks have difficulty dealing with the additional heat generated by hard-switching due to load fluctuations or capacitive loads. Continuous hard-switching results in a temperature rise in the transistor, and excessive heat may damage or destroy the transistors.

B. DIFFICULTIES IN CANCELING CAPACITIVE IMPEDANCE

Impedance matchers are useful for capacitive load cancellation but are not perfect for fluctuating loads. RF plasma systems typically implement mechanical matchers with motor-driven variable capacitors or inductors [26]. However, the mechanical matcher has a problem of slow response. If a switch-mode inverter is used as the RF power source for the plasma system, hard-switching [25] may continue until the matching operation is completed. This long hard-switching continuation will cause damage to the inverter.

C. DIFFICULTIES OF LOAD ESTIMATION FOR INVERTER CONTROL

Despite the above difficulties, efforts to apply switch-mode inverters to RF plasma systems are progressing little by little. Recently, a limited number of prior studies have aimed to prevent hard-switching through frequency control [4] or auxiliary active inductive circuits [17], [18]. These methods need to be operated when the load becomes capacitive and controlled according to the load impedance.

Therefore, the controls require load estimation. In a general kHz-frequency power electronics system, the load impedance value is estimated by observing voltage and current. However, in MHz RF applications, a new problem arises that such load estimation is difficult. This is due to the bandwidth limitations and phase errors in the current and voltage sensors.

III. SCHEME OF PROPOSED SYSTEM

The proposed observation method estimates the load parameters based on the RF traveling and reflected waves instead of voltage and current. These waves are monitored with a directional coupler inserted into the RF output power line. The load impedance value is estimated from the wave powers and the phase difference between these waves.

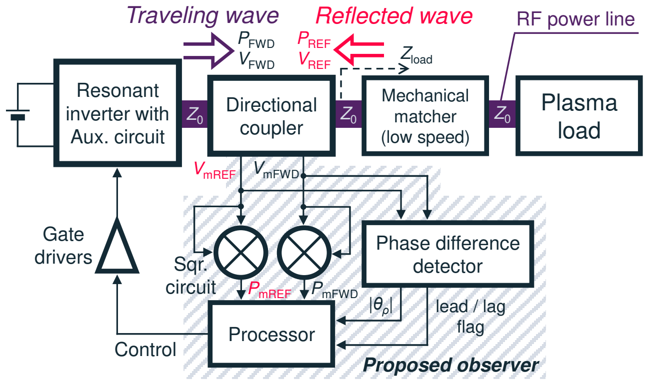

FIGURE 1. Schematic diagram of the control system using the proposed observer.

The proposed method is able to detect the occurrence of capacitive load, and the observation results can be immediately used for the inverter soft-switching control to prevent hard-switching. This makes inverters applicable to RF plasma applications with fluctuating loads. Fig. 1 shows the configuration of the novel inverter control system including the proposed observer. The flow of operation is as follows.

First, in the proposed observer, the traveling and reflected waves are monitored in real time with the directional coupler.

Second, RF voltage multiplier circuits calculate the traveling wave power P_{FWD} and the reflected wave power P_{REF}. Simultaneously, a phase difference detection circuit measures a reflection phase angle θ_ρ i.e., a phase difference of the reflected wave with respect to the traveling wave. θ_ρ leads if the reflection is due to an inductive load and lags if the reflection is due to a capacitive load. Utilizing this nature, inductive load and capacitive load can be distinguished.

Next, when the capacitive load is detected by the phase difference detection circuit, a subsequent processor calculates the complex reflection coefficient ρ from P_{FWD}, P_{REF}, and θ_ρ. ρ is directly related to the load impedance condition.

Finally, an operating amount of the control is determined from ρ, and the auxiliary switched-inductor of the inverter is operated. This operation cancels the leading current due to the capacitive load and allows the inverter to operate in soft-switching mode. As a result, this control protects the inverter from the capacitive load.

IV. PRINCIPLE OF LOAD IMPEDANCE ESTIMATION

This section will describe the theory of obtaining load impedance value from traveling and reflected waves rather than voltage and current. The proposed method uses two key parameters: the reflection coefficient Γ and the reflection phase angle θ_ρ. The former is the ratio of the intensities of these waves, and the latter is the phase difference of the reflected wave with respect to the traveling wave.

The load impedance can be calculated from Γ and θ_ρ. Interestingly, inductive and capacitive loads can be easily distinguished by the positive/negative sign of the reflection phase angle.

A. TRAVELING WAVE AND REFLECTED WAVE

As it is well known in RF electronics, energy propagates between the RF power source and the load as traveling and reflected waves in a transmission cable. A reflected wave always occurs when the load impedance does not match the characteristic impedance of the transmission cable. Hence, the power P_{load} consumed by the load is the difference between the traveling wave power P_{FWD} and the reflected wave power P_{REF} as shown in (1).

$$P_{\mathrm{load}} = P_{\mathrm{FWD}} - P_{\mathrm{REF}} \tag{1}$$

Note that P_{FWD} and P_{REF} are defined as (2) and (3), respectively.

$$P_{\mathrm{FWD}} = V_{\mathrm{FWD}} I_{\mathrm{FWD}} = V_{\mathrm{FWD}}{}^2/Z_0 \tag{2}$$

$$P_{\mathrm{REF}} = V_{\mathrm{REF}} I_{\mathrm{REF}} = V_{\mathrm{REF}}{}^2/Z_0 \tag{3}$$

In (2) and (3), V_{FWD} and I_{FWD} are the voltage and current of the traveling wave, and V_{REF} and I_{REF} are the voltage and current of the reflected wave, respectively. Z_0 is the characteristic impedance of the transmission cable, and the wave voltage/current relationships (4) and (5) always hold. Z_0 is typically a real value 50Ω.

$$V_{\mathrm{FWD}} = Z_0 I_{\mathrm{FWD}} \tag{4}$$

$$V_{\mathrm{REF}} = Z_0 I_{\mathrm{REF}} \tag{5}$$

In general terms, energies and intensities of propagating waves are necessarily defined by the characteristic impedance Z_0.

B. CALCULATION OF LOAD IMPEDANCE FROM REFLECTION COEFFICIENT

The load impedance value can be obtained or estimated based on the wave reflection. The reflection is described by a reflection coefficient and a reflection phase angle.

First, the magnitude Γ of the reflection coefficient is the ratio of intensity of the reflected wave to the traveling wave. Therefore, Γ can be obtained from the wave voltages or powers as (6).

$$\Gamma = |\rho| = \left|\frac{(Reflected\ wave)}{(Traveling\ wave)}\right| = \left|\frac{V_{\mathrm{REF}}}{V_{\mathrm{FWD}}}\right| = \sqrt{\frac{P_{\mathrm{REF}}}{P_{\mathrm{FWD}}}} \tag{6}$$

In (6), ρ is the complex reflection coefficient defined as (7). ρ consists of a real part Re[ρ] and an imaginary part Im[ρ] and is expressed using Γ and a reflection phase angle θ_ρ as in (7).

$$\rho = \mathrm{Re}[\rho] + j\mathrm{Im}[\rho] = \Gamma\cos\theta_\rho + j\Gamma\sin\theta_\rho \quad (-\pi \le \theta_\rho \le \pi) \tag{7}$$

θ_ρ denotes the phase angle of the reflected wave with reference to the traveling wave. j is the imaginary unit.

Second, ρ can be expressed using the complex load impedance Z_{load}. As can be seen from the voltage and current directions defined in Fig. 2, the load voltage V_{load} is the sum of the traveling and reflected wave voltages, and the load current I_{load} is the difference between the traveling and reflected wave currents. Therefore, dividing (1) into voltages and currents, V_{load} and I_{load} are defined as (8) and (9). (9) can be rewritten as (10) by substituting (4) and (5).

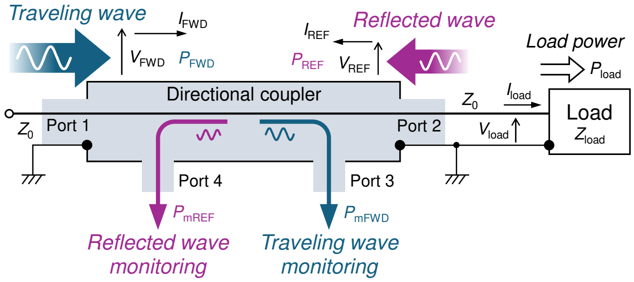

FIGURE 2. Schematic diagram of the typical directional coupler and the traveling and reflected waves.

$$V_{\mathrm{load}} = V_{\mathrm{FWD}} + V_{\mathrm{REF}} \tag{8}$$

$$I_{\mathrm{load}} = I_{\mathrm{FWD}} - I_{\mathrm{REF}} \tag{9}$$

$$= \frac{V_{\mathrm{FWD}}}{Z_0} - \frac{V_{\mathrm{REF}}}{Z_0} \tag{10}$$

The load impedance as a complex number Z_{load} is defined by Ohm's law as (11) using V_{load} and I_{load}.

$$Z_{\mathrm{load}} = V_{\mathrm{load}}/I_{\mathrm{load}} \tag{11}$$

(11) can be rewritten as (12) by substituting (8) and (10).

$$Z_{\mathrm{load}} = \frac{V_{\mathrm{FWD}} + V_{\mathrm{REF}}}{V_{\mathrm{FWD}} - V_{\mathrm{REF}}} Z_0 \tag{12}$$

(12) can be transformed into (13) for V_{REF} and V_{FWD}.

$$V_{\mathrm{REF}}(Z_{\mathrm{load}} + Z_0) = V_{\mathrm{FWD}}(Z_{\mathrm{load}} - Z_0) \tag{13}$$

Solving (13) for $\rho=V_{\mathrm{REF}}/V_{\mathrm{FWD}}$ in (6), ρ is expressed as (14) using Z_{load} and Z_0.

$$\rho = \frac{V_{\mathrm{REF}}}{V_{\mathrm{FWD}}} = \frac{Z_{\mathrm{load}} - Z_0}{Z_{\mathrm{load}} + Z_0} \tag{14}$$

Next, from here, the formula transformations to derive the load impedance will be described. For convenience, the load impedance Z_{load} is commonly expressed as $Z_{\mathrm{load}}=R_{\mathrm{load}}+jX_{\mathrm{load}}$, where R_{load} is the real part representing the resistance component, and X_{load} is the imaginary part representing the reactance component at the wave frequency. By substituting $R_{\mathrm{load}}+jX_{\mathrm{load}}$ for Z_{load} in (14) and then multiplying the numerator and denominator by the complex conjugate of the denominator to make the denominator real, (14) is rewritten as (15) using R_{load} and X_{load}.

$$\begin{aligned}\rho &= \frac{(R_{\mathrm{load}} + jX_{\mathrm{load}}) - Z_0}{(R_{\mathrm{load}} + jX_{\mathrm{load}}) + Z_0} \\ &= \frac{(R_{\mathrm{load}} - Z_0 + jX_{\mathrm{load}})(R_{\mathrm{load}} + Z_0 - jX_{\mathrm{load}})}{(R_{\mathrm{load}} + Z_0 + jX_{\mathrm{load}})(R_{\mathrm{load}} + Z_0 - jX_{\mathrm{load}})} \\ &= \frac{R_{\mathrm{load}}{}^2 - Z_0{}^2 + X_{\mathrm{load}}{}^2 + 2jZ_0X_{\mathrm{load}}}{(R_{\mathrm{load}} + Z_0)^2 + X_{\mathrm{load}}{}^2}\end{aligned} \tag{15}$$

Then, (15) can be decomposed into the real part Re[ρ] and the imaginary part Im[ρ] as shown in (16).

$$\begin{aligned}\mathrm{Re}[\rho] &= \frac{R_{\mathrm{load}}{}^2 - Z_0{}^2 + X_{\mathrm{load}}{}^2}{(R_{\mathrm{load}} + Z_0)^2 + X_{\mathrm{load}}{}^2} \\ \mathrm{Im}[\rho] &= \frac{2Z_0X_{\mathrm{load}}}{(R_{\mathrm{load}} + Z_0)^2 + X_{\mathrm{load}}{}^2}\end{aligned} \tag{16}$$

Finally, the load resistance R_{load} and reactance X_{load} are derived as (17) by solving (16) for R_{load} and X_{load}.

$$R_{\text{load}} = Z_0 \frac{1 - \text{Re}[\rho]^2 - \text{Im}[\rho]^2}{(1 - \text{Re}[\rho])^2 + \text{Im}[\rho]^2}$$
$$X_{\text{load}} = Z_0 \frac{2\text{Im}[\rho]}{(1 - \text{Re}[\rho])^2 + \text{Im}[\rho]^2} \quad (17)$$

Substituting (7) into (17) yields (18).

$$R_{\text{load}} = Z_0 \frac{1 - \Gamma^2}{1 - 2\Gamma \cos\theta_\rho + \Gamma^2}$$
$$X_{\text{load}} = Z_0 \frac{2\Gamma \sin\theta_\rho}{1 - 2\Gamma \cos\theta_\rho + \Gamma^2} \quad (18)$$

To summarize the above, the value of Γ is obtained from V_{FWD} and V_{REF}, and the value of the load impedance can be estimated using Γ and θ_ρ without measuring current.

C. MEASUREMENT OF WAVE POWERS AND REFLECTION COEFFICIENT

As shown in (6), the reflection coefficient Γ can be obtained from the traveling wave power P_{FWD} and the reflected wave power P_{REF}. Here, wave monitoring using a directional coupler and calculation of the coupling coefficient are described.

A directional coupler is a device that can monitor traveling and reflected waves in real time. When a directional coupler is inserted in the RF power transmission line as shown in Fig. 1 of Section 3, the traveling and reflected waves are weakly coupled to the monitor output ports. Then, a small portion of each wave leaks out separately through each monitor output port as shown in Fig. 2. In an ideal directional coupler, the monitor output waveform would be identical to the waveforms of the original traveling and reflected waves. Also, the relationships between P_{FWD}, P_{REF}, and the small powers P_{mFWD} and P_{mREF} of the monitor output waves are as shown in (19) and (20).

$$P_{\text{mFWD}} = k_{\text{p}} P_{\text{FWD}} \quad (19)$$
$$P_{\text{mREF}} = k_{\text{p}} P_{\text{REF}} \quad (20)$$

Therefore, the ratio of P_{mFWD} and P_{mREF} is equal to the ratio of P_{FWD}, P_{REF} respectively. In (19) and (20), k_{p} is the power coupling coefficient of the directional coupler as $k_{\text{p}} \ll 1$.

For accurate monitoring, each monitor output port of the directional coupler must be terminated with a resistor whose resistance is equal to Z_0. This will be described in Section 5. In this configuration, the power of each monitor output wave is equal to the power consumed by each termination resistor. Therefore, P_{mFWD} and P_{mREF} are obtained as (21) and (22) using Z_0 and the root mean square (RMS) voltages $|V_{\text{mFWD}}|$ and $|V_{\text{mREF}}|$ of the terminating resistors.

$$P_{\text{mFWD}} = |V_{\text{mFWD}}|^2 / Z_0 \quad (21)$$
$$P_{\text{mREF}} = |V_{\text{mREF}}|^2 / Z_0 \quad (22)$$

By applying (19) and (20) to (6) and substituting (21) and (22), the value of Γ can be obtained as (23) using monitored P_{mFWD} and P_{mREF}.

$$\Gamma = \sqrt{\frac{P_{\text{mREF}}}{P_{\text{mFWD}}}} = \sqrt{\frac{|V_{\text{mREF}}|^2}{|V_{\text{mFWD}}|^2}} \quad (23)$$

D. RELATIONSHIP BETWEEN REFLECTION PHASE ANGLE AND LOAD REACTANCE

When the load is reactive, a phase difference occurs between the reflected wave and the traveling wave. The reflection phase angle θ_ρ in (7) and (18) represents this phase difference. The positive/negative sign of θ_ρ directly depends on whether the load is inductive or capacitive.

As shown in (7), observing θ_ρ is required to derive the complex reflection coefficient ρ. θ_ρ can be obtained by measuring the time difference t_ρ between the reflected wave and the traveling wave using a phase difference detection circuit. t_ρ and θ_ρ have a relation of (24) using the period T of the waves.

$$\frac{t_\rho}{T} = \frac{\theta_\rho}{2\pi} \quad (24)$$

(24) is expressed as (25) using the angular frequency ω of the waves.

$$\theta_\rho = \omega t_\rho \quad (25)$$

Next, since θ_ρ is the phase angle of the complex reflection coefficient ρ, it can be expressed using the relationship between the real part and the imaginary part of ρ. θ_ρ is expressed as (26) using the impedances by substituting (16).

$$\theta_\rho = \tan^{-1}\left(\frac{\text{Im}[\rho]}{\text{Re}[\rho]}\right)$$
$$= \tan^{-1}\left(\frac{2Z_0 X_{\text{load}}}{R_{\text{load}}{}^2 - Z_0{}^2 + X_{\text{load}}{}^2}\right) \quad (26)$$

According to (26), an inductive load, i.e., a positive X_{load}, causes phase leading in θ_ρ, whereas a capacitive load, i.e., negative X_{load}, causes phase lagging in θ_ρ.

Therefore, the positive/negative sign of θ_ρ can be used to identify whether the load is inductive or capacitive. The proposed observation system utilizes this property to detect capacitive loads and control the inverter system to avoid hard-switching. Range of θ_ρ and the relations between the reflection phase and the load condition are summarized in Table 1.

TABLE I
RELATIONSHIP BETWEEN LOAD REACTANCE CONDITION AND PHASE ANGLE OF REFLECTED WAVE

Load reactance	Phase of reflected wave with reference to traveling wave	Range of θ_ρ
Inductive	Leading	$0 < \theta_\rho < \pi$
Capacitive	Lagging	$-\pi < \theta_\rho < 0$

V. EXPERIMENTAL PROTOTYPE OF PROPOSED SYSTEM

This section will describe the circuit configuration and operating principles of the experimental system. A prototype was fabricated to verify the concept of the proposed measurement method and to demonstrate the soft-switching control under capacitive load.

An auxiliary switched-inductor is connected to a 3.75MHz full-bridge inverter to prevent hard-switching. This switched-inductor is the controlled target of the experimental system and will be controlled when the proposed observer detects a capacitive load.

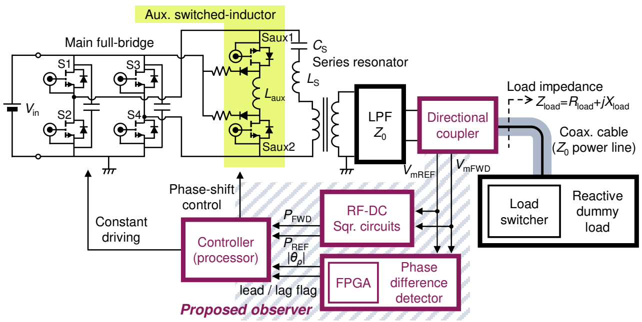

FIGURE 3. Schematic diagram of the total experimental system.

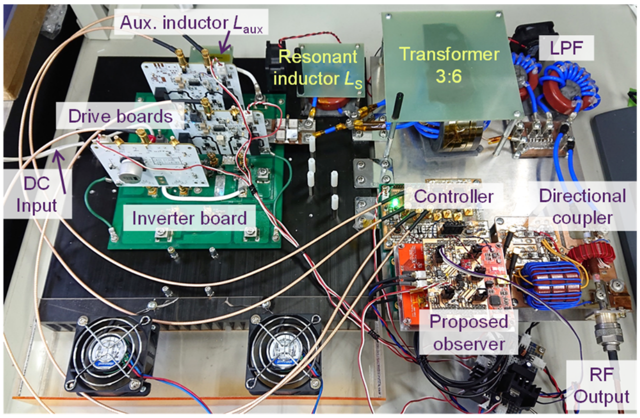

FIGURE 4. Experimental prototype of the proposed system.

Fast response capability is key to dealing with not only steady capacitive loads but also dynamic load changes from inductive to capacitive. The directional coupler is a real-time sensing component. A high-speed FPGA was employed to obtain the reflection phase angle, and a high-speed microprocessor was employed to calculate the operation amount and to operate the phase-shift control of the switched-inductor. These allow the inverter to transition quickly from hard-switching to soft-switching, thus protecting the inverter.

Fig. 3 shows the schematic diagram of the total experimental system. Each experimental component of the proposed observer is discussed below. The prototype system is shown in Fig. 4.

A. TANDEM-MATCH DIRECTIONAL COUPLER

The directional coupler in the experimental prototype employs a tandem-match topology [23], [27] with four ports as shown in Fig. 5(a). Ports 1 and 2 are the input and output ports for RF power to pass through, and the others are coupled output signal ports for wave monitoring. Port 3 couples with the traveling wave, and Port 4 couples with the reflected wave. These waves are monitored simultaneously on a single circuit using the same principle with the same gain.

From here, the wave observation principle and circuit design formulas of the tandem-match coupler will be explained. As shown in Fig. 5(a), the tandem-match coupler has a current transformer and a voltage transformer. The connection between Ports 1 and 2 is the primary circuit, and the resistor network including Ports 3 and 4 is the secondary circuit of the transformers.

Fig. 5(b) shows the ideal equivalent circuit of the secondary circuit. The resistance R_0 in Fig. 5(b) is the equivalent combined resistance of the resistor network at node A or node B. For highly accurate load estimation in the proposed system, it is necessary to monitor the ratio of the traveling and reflected waves with high precision by making the monitor gains for these waves equal. This gain equalization can be achieved by making R_0 of nodes A and B exactly equal. With the parameter in Fig. 5(a), the resistance is R_0=(50+60)//120=57.39Ω because Ports 3 and 4 are each terminated with 50Ω by the subsequent phase difference detection circuit described later.

When RF load voltage V_{load} and current I_{load} shown in Fig. 2 are applied to the primary circuit, voltage V_{VT} is induced on the secondary side of the voltage transformer as (27), and current I_{CT} is induced on the secondary side of the current transformer as (28).

$$V_{VT} = k_{VT}\frac{V_{load}}{N_{VT}} \tag{27}$$

$$I_{CT} = k_{CT}\frac{I_{load}}{N_{CT}} \tag{28}$$

In (27) and (28), k_{VT} and k_{CT} are the coupling coefficients of the respective transformers, and N_{VT} and N_{CT} are the turns ratios of the respective transformers as N_{VT}:1 and 1:N_{CT}.

Since the secondary circuit has both voltage and current sources, it can be decomposed into two equivalent circuits, as illustrated in Figs. 5(c) and 5(d). These circuits are analyzed independently and subsequently recombined via the superposition theorem. Specifically, the circuit in Fig. 5(c) contains only a voltage source V_{VT}, and the circuit in Fig. 5(d) contains only a current source I_{CT}.

To explain the circuit operation, the calculations focus on the voltages at nodes A and B. In the circuit in Fig. 5(c), voltages V_{Av} and V_{Bv} are produced at nodes A and B as (29)

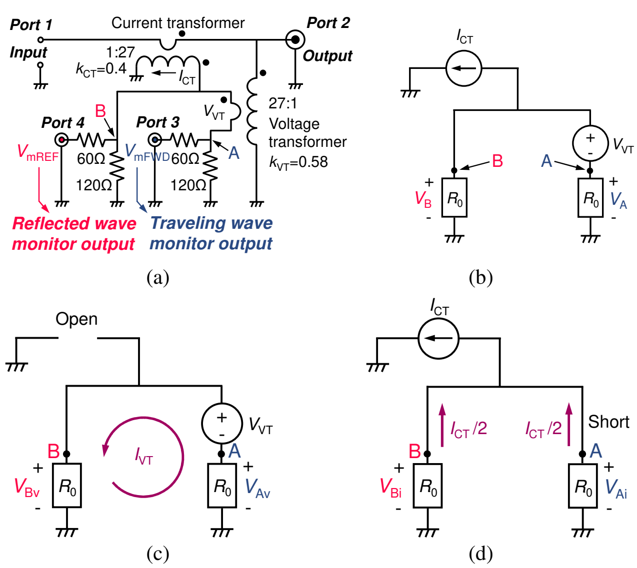

FIGURE 5. Tandem-match directional coupler.
(a) Circuit diagram, (b) Equivalent circuit of the secondary network, (c) Open the current source, (d) Short the voltage source.

due to voltage division by R_0. On the other hand, in the circuit in Fig. 5(d), voltages V_{Ai} and V_{Bi} are produced at nodes A and B as (30) due to voltage drop by R_0.

$$V_{\mathrm{Av}} = -V_{\mathrm{Bv}} = -V_{\mathrm{VT}}/2 \tag{29}$$

$$V_{\mathrm{Ai}} = V_{\mathrm{Bi}} = -R_0 I_{\mathrm{CT}}/2 \tag{30}$$

By applying the superposition theorem to the voltage-source circuit and the current-source circuit, the voltages at nodes A and B are represented as (31) and (32), respectively.

$$V_{\mathrm{A}} = V_{\mathrm{Av}} + V_{\mathrm{Ai}} = -\frac{1}{2}(V_{\mathrm{VT}} + R_0 I_{\mathrm{CT}}) \tag{31}$$

$$V_{\mathrm{B}} = V_{\mathrm{Bv}} + V_{\mathrm{Bi}} = \frac{1}{2}(V_{\mathrm{VT}} - R_0 I_{\mathrm{CT}}) \tag{32}$$

Substituting (27) and (28) into (31) and (32), V_{A} and V_{B} are expressed as (33) and (34), respectively.

$$V_{\mathrm{A}} = -\frac{1}{2}\left(k_{\mathrm{VT}}\frac{V_{\mathrm{load}}}{N_{\mathrm{VT}}} + k_{\mathrm{CT}}R_0\frac{I_{\mathrm{load}}}{N_{\mathrm{CT}}}\right) \tag{33}$$

$$V_{\mathrm{B}} = \frac{1}{2}\left(k_{\mathrm{VT}}\frac{V_{\mathrm{load}}}{N_{\mathrm{VT}}} - k_{\mathrm{CT}}R_0\frac{I_{\mathrm{load}}}{N_{\mathrm{CT}}}\right) \tag{34}$$

Designed as $N_{\mathrm{VT}}=N_{\mathrm{CT}}=N$, (33) and (34) are expressed as (35) and (36), respectively.

$$V_{\mathrm{A}} = -\frac{k_{\mathrm{VT}}}{2N}\left(V_{\mathrm{load}} + \frac{k_{\mathrm{CT}}}{k_{\mathrm{VT}}}R_0 I_{\mathrm{load}}\right) \tag{35}$$

$$V_{\mathrm{B}} = \frac{k_{\mathrm{VT}}}{2N}\left(V_{\mathrm{load}} - \frac{k_{\mathrm{CT}}}{k_{\mathrm{VT}}}R_0 I_{\mathrm{load}}\right) \tag{36}$$

Here, the resistor networks not only functions as R_0 for voltage/current synthesis shown in (31) to (36), but also as voltage dividers for limiting the voltages of Ports 3 and 4. With 60Ω and the above termination of 50Ω, the monitor output voltages V_{mFWD} and V_{mREF} at Ports 3 and 4 are the attenuated voltage of V_{A} and V_{B} as shown in (37) and (38), respectively

$$\begin{aligned} V_{\mathrm{mFWD}} &= \frac{50}{50+60}V_{\mathrm{A}} \\ &= -k_0\left(V_{\mathrm{load}} + \frac{k_{\mathrm{CT}}}{k_{\mathrm{VT}}}R_0 I_{\mathrm{load}}\right) \end{aligned} \tag{37}$$

$$\begin{aligned} V_{\mathrm{mREF}} &= \frac{50}{50+60}V_{\mathrm{B}} \\ &= k_0\left(V_{\mathrm{load}} - \frac{k_{\mathrm{CT}}}{k_{\mathrm{VT}}}R_0 I_{\mathrm{load}}\right) \end{aligned} \tag{38}$$

where k_0 is a gain coefficient as in (39).

$$k_0 = \frac{50}{50+60} \times \frac{k_{\mathrm{VT}}}{2N} \tag{39}$$

Finally, the relationship between the monitorable V_{mFWD} and the original traveling wave voltage V_{FWD}, and the relationship between the monitorable V_{mREF} and the original reflected wave voltage V_{REF} will be derived. Substituting (8) and (10) into V_{load} and I_{load}, (37) and (38) can be rewritten as (40) and (41), respectively.

$$V_{\mathrm{mFWD}} = -k_0\left(V_{\mathrm{FWD}} + V_{\mathrm{REF}} + \frac{k_{\mathrm{CT}}R_0}{k_{\mathrm{VT}}Z_0}(V_{\mathrm{FWD}} - V_{\mathrm{REF}})\right) \tag{40}$$

$$V_{\mathrm{mREF}} = k_0\left(V_{\mathrm{FWD}} + V_{\mathrm{REF}} - \frac{k_{\mathrm{CT}}R_0}{k_{\mathrm{VT}}Z_0}(V_{\mathrm{FWD}} - V_{\mathrm{REF}})\right) \tag{41}$$

When k_{CT}, k_{VT}, and R_0 are designed as (42) considering Z_0 of the RF power line,

$$\frac{k_{\mathrm{CT}}}{k_{\mathrm{VT}}}R_0 = Z_0 \tag{42}$$

some terms of (40) and (41) are cancelled out, and V_{mFWD} and V_{mREF} are simply expressed as (43) and (44), respectively.

$$V_{\mathrm{mFWD}} = -2k_0 V_{\mathrm{FWD}} \tag{43}$$

$$V_{\mathrm{mREF}} = 2k_0 V_{\mathrm{REF}} \tag{44}$$

Hence, the RMS voltages appearing at Ports 3 and 4 are expressed as (45) and (46), indicating that the traveling and reflected wave voltages can be monitored via k_0.

$$|V_{\mathrm{mFWD}}| = 2k_0|V_{\mathrm{FWD}}| \tag{45}$$

$$|V_{\mathrm{mREF}}| = 2k_0|V_{\mathrm{REF}}| \tag{46}$$

Based on V_{FWD} and V_{REF}, the traveling wave power P_{FWD} and the reflected wave power P_{REF} can be estimated using the RF-DC voltage squaring circuits described later.

B. TEST OF PROTOTYPE DIRECTIONAL COUPLER

The measured parameters of the prototype tandem-match coupler are listed in Table 2. In the voltage transformer, the primary winding impedance is designed to be sufficiently higher than the characteristic impedance Z_0=50Ω of the RF output power line. In addition, to reduce the influences on the line, k_{CT} is designed to be low and k_{VT} to be high.

The directivity (i.e., directional wave extraction characteristic) of the coupler was examined. During the measurements, Ports 3 and 4 were terminated with 50Ω RF resistors.

1) Test 1: to verify the directivity to extract traveling wave, a 3.75MHz sinusoidal wave was injected from Port 1 to Port 2, and the outputs of Ports 3 and 4 were measured. Port 2 was terminated with a 50Ω load resistor.
2) Test 2: to verify the directivity to extract reflected wave, a 3.75MHz sinusoidal wave was injected from Port 2 to Port 1, and the outputs of Ports 3 and 4 were measured. Port 1 was terminated with a 50Ω load resistor.

TABLE II
MEASURED PARAMETERS OF THE PROTOTYPE DIRECTIONAL COUPLER

Component	Parameter	Value at 3.75MHz
Current transformer	Secondary self-inductance (μH)	8.37
	Secondary absolute impedance (Ω)	197.3
	Coupling coefficient k_{CT}	0.4
	Number of turn ratio	1:27
Voltage transformer	Primary self-inductance (μH)	26.18
	Secondary self-inductance (μH)	0.092
	Primary absolute impedance (Ω)	617.2
	Secondary absolute impedance (Ω)	2.17
	Coupling coefficient k_{VT}	0.58
	Number of turn ratio	27:1

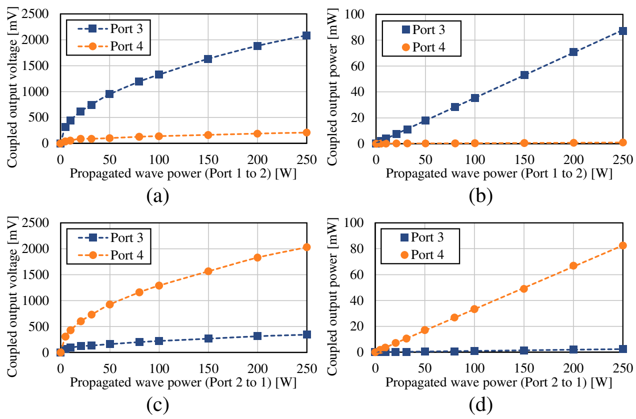

FIGURE 6. **Measured characteristics of the prototype directional coupler.**
(a) Ports 3 and 4 voltages when power is propagated from Port 1 to 2,
(b) Ports 3 and 4 powers calculated from (a) with termination Z_0,
(c) Ports 3 and 4 voltages when power is propagated from Port 2 to 1,
(d) Ports 3 and 4 powers calculated from (c) with termination Z_0.

The results of Tests 1 and 2 are shown in Figs. 6(a) to 6(d). Fig. 6(a) shows the output RMS voltages at Ports 3 and 4 in Test 1. The Port 4 voltage is sufficiently low compared to the Port 3 voltage. Fig. 6(b) shows the RF powers at Ports 3 and 4 calculated from voltages and the termination 50Ω. Most of the power appears in Port 3, and the power mixed in Port 4 is sufficiently small. This result means that the traveling wave power can be monitored at Port 3. In addition, Fig. 6(b) shows good linearity of power extraction characteristics of the prototype directional coupler. The Port 3 power is proportional to the RF power propagating from Port 1 to Port 2.

Figs. 6(c) and 6(d) show the output RMS voltages and powers at Ports 3 and 4 in Test 2. The voltage and power of Port 4 are high, whereas those of Port 3 are sufficiently low. In other words, the directivity was confirmed even for reverse power propagation.

From Tests 1 and 2, it was confirmed that the traveling wave and the reflected wave could be clearly separated and observed at Ports 3 and 4.

C. RF-DC VOLTAGE SQUARING CIRCUITS

The wattages of the monitored RF waves are obtained as DC values by using voltage squaring circuits. Real-time RF voltage squaring is enabled by an analog multiplier IC. Each wave from Ports 3 and 4 of the directional coupler is simultaneously input to each one squaring circuit.

Squaring (45) and (46) respectively yields (47) and (48) using P_{FWD} and P_{REF} in (2) and (3).

$$\begin{aligned}|V_{\mathrm{mFWD}}|^2 &= 4{k_0}^2|V_{\mathrm{FWD}}|^2\\ &= 4{k_0}^2 Z_0 P_{\mathrm{FWD}}\end{aligned} \tag{47}$$

$$\begin{aligned}|V_{\mathrm{mREF}}|^2 &= 4{k_0}^2|V_{\mathrm{REF}}|^2\\ &= 4{k_0}^2 Z_0 P_{\mathrm{REF}}\end{aligned} \tag{48}$$

By transforming (47) and (48) respectively, the values of P_{FWD} and P_{REF} can be found as (49) and (50) using V_{mFWD} and V_{mREF}.

$$P_{\mathrm{FWD}} = \frac{|V_{\mathrm{mFWD}}|^2}{4{k_0}^2 Z_0} \tag{49}$$

$$P_{\mathrm{REF}} = \frac{|V_{\mathrm{mREF}}|^2}{4{k_0}^2 Z_0} \tag{50}$$

Here, the actual inputs are time-changing voltages of waves. Since the phase difference between these waves is equal to the phase difference θ_ρ between the traveling and reflected waves, the monitor waves can be expressed as (51) and (52) using θ_ρ.

$$v_{\mathrm{mFWD}} = -\sqrt{2}|V_{\mathrm{mFWD}}|\sin\omega t \tag{51}$$

$$v_{\mathrm{mREF}} = \sqrt{2}|V_{\mathrm{mREF}}|\sin(\omega t + \theta_\rho) \tag{52}$$

Negative sign in (51) means waveform inversion due to tandem-match topology, similarly to (43).

The waveform voltages v_{mFWD} and v_{mREF} are squared in the circuit as (53) and (54), respectively.

$$\begin{aligned}{v_{\mathrm{mFWD}}}^2 &= 2|V_{\mathrm{mFWD}}|^2\sin^2\omega t\\ &= |V_{\mathrm{mFWD}}|^2 - |V_{\mathrm{mFWD}}|^2\cos 2\omega t\end{aligned} \tag{53}$$

$$\begin{aligned}{v_{\mathrm{mREF}}}^2 &= 2|V_{\mathrm{mREF}}|^2\sin^2(\omega t + \theta_\rho)\\ &= |V_{\mathrm{mREF}}|^2 - |V_{\mathrm{mREF}}|^2\cos 2(\omega t + \theta_\rho)\end{aligned} \tag{54}$$

The time changing items $|V_{\mathrm{mFWD}}|^2\cos 2\omega t$ and $|V_{\mathrm{mREF}}|^2\cos 2(\omega t+\theta_\rho)$ in (53) and (54) can be averaged as zero and eliminated by using a small low-pass filter (LPF). Therefore, steady components $|V_{\mathrm{mFWD}}|^2$ and $|V_{\mathrm{mREF}}|^2$ are output as DC voltages from the squaring circuits.

The prototype squaring circuit uses an AD834ARZ analog multiplier IC. Fig. 7 shows the circuit diagram of the single squaring circuit. The squared output is DC voltage and is read by the subsequent microprocessor described later. Then, the reflection coefficient Γ is obtained by applying the output values of the squaring circuits to (23).

Two squaring circuits are connected to Ports 3 and 4 of the directional coupler by 50Ω coaxial cables, respectively. The length of each cable is 200mm, which is sufficiently shorter than the wavelength at 3.75MHz. Fig. 8 shows the measured input-to-output voltage characteristic of the prototype squaring circuit.

Next, the input-to-output characteristics of the entire power observation path, including the directional coupler and the squaring circuit, were also measured. Fig. 9(a) shows the

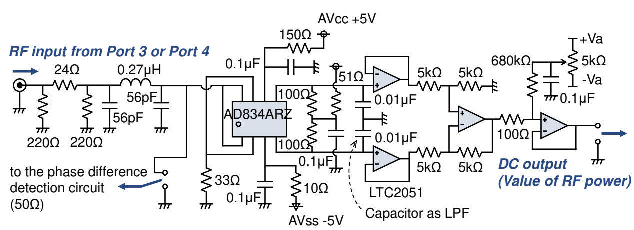

FIGURE 7. **Circuit diagram of the single RF-DC voltage squaring circuit using an AD834ARZ analog multiplier IC.**

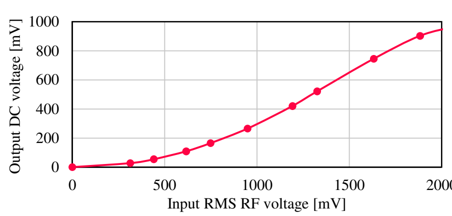

FIGURE 8. **Input-to-output voltage characteristic of the RF-DC voltage squaring circuit.**

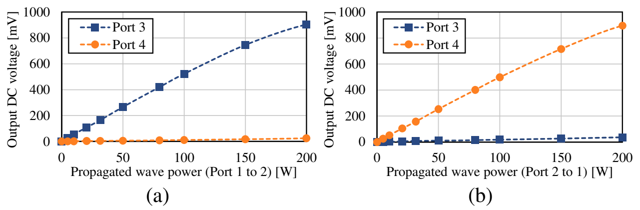

FIGURE 9. Characteristics of the total power observation paths including the directional coupler and squaring circuits. (a) Output DC voltages when RF power is propagated from Port 1 to 2, (b) Output DC voltages when RF power is propagated from Port 2 to 1.

results of the DC output voltages versus the propagated RF power in the directional coupler from Port 1 to 2. Fig. 9(b) shows the DC output voltages versus the propagated RF power in the directional coupler from Port 2 to 1. Therefore, the powers of traveling and reflected waves are monitored according to the characteristics in Figs. 9(a) and 9(b).

Linearity is important in power observation. The inverter control experiments, which will be described in Section 7, were conducted in the sub-100W region, where the prototype squaring circuit has good linearity as in Figs. 9(a) and 9(b).

D. PHASE DIFFERENCE DETECTION CIRCUIT

Phase difference θ_p between the 3.75MHz sinusoidal waves v_{mFWD} and v_{mREF} from the directional coupler are monitored by the phase difference detection circuit. This circuit is connected to Ports 3 and 4 of the directional coupler as shown in Figs. 1 and 3. Fig. 10 shows the schematic diagram of the prototype phase difference detection circuit devised in this study. The concept of this circuit is to convert the phase difference into the voltage of a capacitor.

The outline of the operation steps are as follows. First, as illustrated in Fig. 10, sinusoidal input waves from Ports 3 and 4 are converted into 3.3V rectangular signals 'FWD' and 'REF', respectively, by the voltage-peak-timing detector for the FPGA to recognize these waves. The rising timing of each signal coincides with the timing of the voltage peak of each original wave. Hence, the phase difference between the waves is preserved as the phase difference of REF and FWD.

Second, the FPGA detects whether the phase of FWD or REF is leading and measures the phase difference between FWD and REF. Through this process, the FPGA recognizes whether the load is inductive or capacitive. The digital flag indicating the phase lead/lag of REF is output from the FPGA and passed to the subsequent control microprocessor.

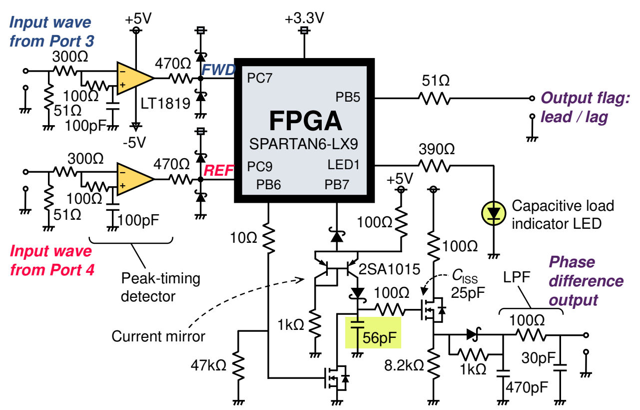

FIGURE 10. Circuit diagram of the phase difference detection circuit designed for the experiment.

Simultaneously, the FPGA operates a constant current circuit 'current mirror' to charge a 56pF ceramic capacitor, and the measured phase difference is converted into a capacitor voltage. The value of the capacitor voltage is exported to the subsequent microprocessor through the voltage-follower transistor and a small LPF as shown in Fig. 10. The microprocessor reads the phase difference angle θ_p from the read voltage and recognizes the load impedance value. The LPF reduces voltage ripples caused by charging and discharging the capacitor.

The prototype circuit uses a LT1819 high-speed comparator IC for the voltage-peak-timing detector and a SPARTAN6-LX9 FPGA for the logic. To count the phase difference of the 3.75MHz signals, the clock frequency of the FPGA was set to 368MHz using a built-in phase-locked loop (PLL). Since 368MHz is approximately 98 times the frequency 3.75MHz of the measured signals, the measurement resolution of the phase difference angle θ_p is 360°/98=3.7°, which is sufficiently fine for proof of concept.

The rectangular signals FWD and REF have two digital states as 0V (State 0) and 3.3V (State 1). The state of FWD and REF is simultaneously monitored by the FPGA as the clock pulse rises. The FPGA counts the elapsed time from when either FWD or REF changes from State 0 to State 1 until the other also changes. This elapsed time corresponds to the phase difference between FWD and REF.

Note that due to the tandem-match topology as in (43) and (51), the lead/lag relationship of REF with respect to FWD is reversed from the lead/lag of the reflected wave with respect to the traveling wave shown in Table 1 in Section 4.

Table 3 shows the truth table of the operations of the FPGA corresponding to the signal states. If REF changes to State 1 before FWD, the FPGA recognizes the load as capacitive; conversely, if FWD changes to State 1 first, it recognizes the load as inductive. If FWD and REF change to State 1 simultaneously, it means a non-reactive load. The output digital flag from the FPGA is '0' when the load is inductive

TABLE III
TRUTH TABLE OF PHASE DETECTION BY FPGA

FWD	REF	Recognition	Output flag	Operation for 56pF capacitor
0 → 0	0 → 0	*	**	***
0 → 1	0 → 1	non-reactive	1	***
0 → 0	0 → 1	capacitive	1	charge
0 → 0	1 → 1	capacitive	1	charge
0 → 1	0 → 0	inductive	0	charge
1 → 1	0 → 0	inductive	0	charge
1 → 1	1 → 1	*	**	***
1 → 1	1 → 0	*	**	discharge
1 → 0	1 → 1	*	**	discharge
1 → 0	1 → 0	*	**	discharge

*ignore
**holding state (no change)
***no operation (stop)
The input signal states are watched and compared to the previous states every 368MHz clock signal.

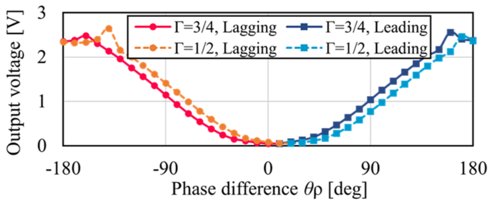

FIGURE 11. Output voltage of the phase difference detection circuit with respect to the phase difference between reflected and traveling waves.

and ‘1’ when the load is capacitive or non-reactive. In the output stage, the current mirror is operated only when the load is recognized as capacitive. The current mirror charges the 56pF capacitor only during the phase difference period.

Fig. 11 shows the measurement result of the output voltage characteristic of the prototype phase difference detection circuit with respect to the input phase difference. Since this voltage indicates the absolute value of θ_ρ (-180°<θ_ρ<180°) as described above, the characteristics are close to a V-shape and the linearity is symmetric with respect to the vertical axis. The linearity is slightly broken around the point θ_ρ=0 due to the non-linearity of the diodes and the FET in the low voltage region. This small error is corrected by a program in the microprocessor connected at the subsequent stage.

E. MICROPROCESSOR TO CALCULATE PHASE-SHIFT CONTROL QUANTITY

The experimental prototype system employs a Piccolo C2000 F28027 micro-processor for generating and controlling gate drive signals. When the phase difference detection circuit detects a capacitive load and outputs the flag ‘1’, this microprocessor calculates and determines the phase-shift control quantity from the values of Γ and θ_ρ. The system clock was set to 60MHz. The F28027 microprocessor has high-resolution pulse width modulation (HR-PWM) modules that allow phase-shift control of MHz-frequency drive signals.

Division is required to calculate the reflection coefficient as in (23) and operate the HR-PWM module. Floating-point arithmetic is generally used for division in computer programs, but its calculation speed is slow. Then, fixed-point arithmetic is employed in this prototype to speed up the divisions.

After Γ is calculated, the phase-shift control quantity is quickly processed by a conditional branching algorithm using an array in the program. The values of the phase-shift quantity are pre-stored in the array and picked out according to Γ and θ_ρ. The detailed operation of the inverter control will be described in the next section.

VI. RESONANT INVERTER AND LOAD FOR EXPERIMENT

This section describes the inverter and dummy load included in Fig. 3 and used to test the proposed system. The inverter consists of the main full-bridge configuration and the controllable auxiliary switched-inductor. The inverter itself was previously developed by some of the authors for 400kHz operation [17], [18]. In this paper, the inverter is updated for MHz-frequency switching using GaN-HEMTs, which are low-loss fast-switching power devices.

Switched-inductors have been commonly used to control kHz-frequency power electronics. Various control techniques using switched-inductors have been developed such as PWM-controlled motor drive and induction heating applications [28]–[31]. Nonetheless, most of their operating frequencies were limited in kHz-frequency bands and rarely used in RF systems. In this study, MHz-frequency operation and control of the switched-inductor became possible by using GaN-HEMTs for the auxiliary switches. The operating frequency of both the full-bridge switch and the switched-inductor is fixed. Therefore, compared to frequency-controlled methods [4], this circuit is more suitable for typical MHz applications with frequency bandwidth limitations imposed by regulation.

A. FULL-BRIDGE INVERTER WITH AUXILIARY SWITCHED-INDUCTOR

Fig. 12 shows the circuit diagram of the inverter. The main full-bridge switches S1–S4 and the auxiliary switches Saux1 and Saux2 consist of GS66516T GaN-HEMTs with reverse-parallel C3D03065E Silicon-Carbide Schottky barrier diodes (SiC-SBD). The output of the full-bridge configuration is connected to an LPF through a series resonator and a step-up transformer. The characteristic impedance of the LPF is designed as Z_0=50Ω, and output power is fed to the load through the 50Ω coaxial cable.

S1–S4 are just driven constantly by the microprocessor through NCP81074A gate driver ICs at 3.75MHz regardless of the load conditions. When the load is inductive, the main-circuit current i_m lags behind the switching timing of S1–S4, establishing soft-switching.

As shown in Fig. 12, the auxiliary switched-inductor is connected in parallel with the full-bridge output terminals to actively compensate the phase of i_m under capacitive load conditions. When the load is estimated as inductive by the proposed observer, Saux1 and Saux2 are kept off, and the switched-inductor does not affect the inverter operation. Whereas, when the load is estimated as capacitive, Saux1 and Saux2 is operated with phase-shift control relative to the switching timing of S1–S4. The phase of i_m is forcibly delayed by the switched-inductor, achieving soft-switching.

Fig. 13 illustrates theoretical waveforms of the inverter under capacitive load. Saux1 and Saux2 are driven at same frequency with S1–S4 but in a different phase. While either S2, S3, and Saux1, or S1, S4, and Saux2 are in the on-state, the

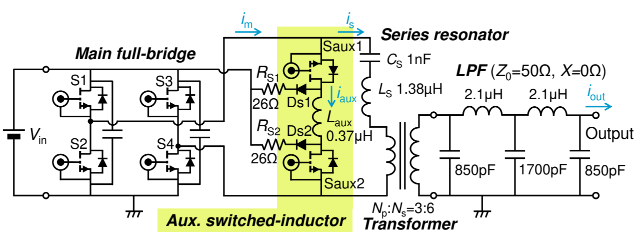

FIGURE 12. Circuit diagram of the resonant soft-switching inverter with the auxiliary switched-inductor.

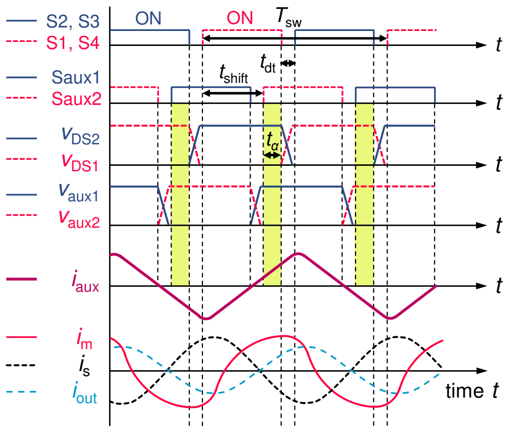

FIGURE 13. **Theoretical waveforms of the main full-bridge and Aux. circuit under capacitive load.**

full-bridge output voltage is applied to the auxiliary inductor L_{aux}. This voltage excites a current i_{aux} in L_{aux} in this period. This 'conduction period' is indicated as t_α in Fig. 13. The amperage of i_{aux} depends on the length of t_α. t_α is properly adjusted by the phase-shift amount t_{shift} of the auxiliary drive signals, which is controlled by the microprocessor according to the measured reflection parameters.

The capacitive load reactance is compensated by i_{aux}, and the equivalent load impedance (seen by the full-bridge switch) becomes inductive. i_{aux} introduces a phase lag in i_m relative to the drain-source voltages of S2 and S3. Consequently, soft-switching is enabled in S1–S4 even if the load is capacitive.

Additionally, since L_{aux} is an inductive component, soft-switching also occurs in Saux1 and Saux2 themselves.

In the microprocessor, a 12-bit analog-to-digital (AD) converter is always in operation to read the output voltages of the squaring circuit and the phase difference detection circuit. The phase-shift control is initiated by the AD conversion complete interrupt. The moving average values of five AD conversions are used to calculate the control amount t_{shift}.

B. PHASE-SHIFT OPERATION BASED ON ESTIMATED LOAD IMPEDANCE

Phase-shift control is performed based on the observed Γ and θ_ρ in accordance with the estimated load in (18). Since the step-up transformer is inserted between the load and the inverter, the characteristics of the transformer affect the impedance seen by the full-bridge switch. Therefore, it is necessary to take the transformer characteristics into account in the phase-shift control. The leakage inductance is canceled by resonance, but the number of turn ratio N_P:N_S has an effect. Hence, the resistance R_{load}' and reactance X_{load}' seen by the full-bridge switch are expressed as (55) using R_{load} and X_{load}.

$$\begin{aligned} R_{load}' &= \frac{N_p^{\,2}}{N_s^{\,2}} R_{load} + R_{es} \\ X_{load}' &= \frac{N_p^{\,2}}{N_s^{\,2}} X_{load} \parallel X_m \\ &= \frac{N_p^{\,2} X_{load} X_m}{N_p^{\,2} X_{load} + N_s^{\,2} X_m} \end{aligned} \tag{55}$$

TABLE IV
MEASURED INPUT IMPEDANCE OF LOAD NETWORK AND REQUIRED PHASE-SHIFT QUANTITY FOR EXAMINED LOAD

Parameter	Symbol	Inductive load	Capacitive load
Load resistance (Ω)	R_{load}	55.30	27.20
Load reactance (Ω)	X_{load}	24.98	-35.35
Input resistance (Ω)	R_{load}'	9.99	10.63
Input reactance (Ω)	X_{load}'	9.37	-7.95
Theoretical conduction period (ns)	t_α	--	35.47
Theoretical required phase-shift (ns)	t_{shift}	--	72.88

TABLE V
'CONDUCTION PERIOD' AT EACH REFLECTION CONDITION

		Reflection phase angle θ_ρ (deg)						
		-10	-30	-60	-90	-120	-150	-170
Reflection coefficient	0.20	3.61	4.62	6.28	7.97	9.27	9.24	8.01
	0.33	3.00	4.35	6.66	9.39	12.30	13.60	11.5
	0.50	2.31	3.90	6.68	10.36	15.59	21.47	19.49
	0.70	1.64	3.33	6.31	10.47	17.50	32.42	42.18
	0.90	1.07	2.78	5.75	9.86	17.12	37.33	102.82

Theoretical values of the conduction period t_α (ns).

TABLE VI
PROGRAMED PHASE-SHIFT QUANTITY FOR EACH REFLECTION CONDITION

		Reflection phase angle θ_ρ (deg)						
		-10	-30	-60	-90	-120	-150	-170
Reflection coefficient	0.20	114.74	113.73	112.07	110.38	109.08	109.11	110.34
	0.33	115.35	114.00	111.69	108.96	106.05	104.75	106.85
	0.50	116.04	114.45	111.67	107.99	102.76	96.88	98.86
	0.70	116.71	115.02	112.04	107.88	100.85	85.93	76.17
	0.90	117.28	115.57	112.60	108.49	101.23	81.02	15.53

Programed values of the phase-shift amount t_{shift} (ns).

In (55), N_p and N_s are primary and secondary turns of the transformer. R_{es} and X_m are equivalent series resistance (ESR) and mutual reactance of the transformer, R_{es}=167.7mΩ and X_m=96.44Ω in the prototype at 3.75MHz. By applying R_{load}' and X_{load}' to the theory reported in [17], [18], theoretical optimal t_α to cancel the capacitive reactance is determined as (56). t_α is shorter than a quarter cycle of the drive signal.

$$t_\alpha = \frac{2\left(R_{load}' - 2X_{load}'\right)}{\pi\left(R_{load}'^{\,2} + X_{load}'^{\,2}\right)} L_{aux} \tag{56}$$

In addition, the practical amount of phase shift quantity t_{shift} directly controlled by the microprocessor as shown in Fig. 13 is expressed as (57)

$$t_{shift} = \frac{T_{sw}}{2} - t_\alpha - t_{dt} \tag{57}$$

where T_{sw} is a cycle of the drive signal. T_{sw} is 266.7ns when the operating frequency is 3.75MHz. The dead time t_{dt}=15.0ns is deducted from t_{shift}.

By applying the above control, the inverter current i_m lags due to L_{aux}, and soft-switching is achieved in S1–S4. The measured R_{load}, X_{load}, R_{load}', and X_{load}' of the experimental setup and the required values of t_α and t_{shift} are listed in Table 4.

Theoretical values of t_α corresponding to the reflection coefficients Γ and the reflection phase angles θ_ρ are listed in Table 5. The required control quantity t_{shift} for each reflection condition is listed in Table 6. In the prototype, the control is performed using t_{shift} in Table 6 according to the observed values Γ and θ_ρ. As mentioned in Section 5, each t_{shift} value in Table 6 is stored in an array in the microprocessor program, and the most suitable value is called according to Γ and θ_ρ.

C. LOAD

In the experiments, either an inductive or capacitive dummy load was applied to the prototype inverter system. Fig. 14 illustrates the schematic diagram of the fabricated variable dummy load. The load consists of a manual load-switcher circuit, a fixed inductive network, and an oil-cooled 50Ω RF resistor. This load-switcher is a high-speed switched-capacitor designed for manual operation. To enable rapid changes in load impedance, GS66516T GaN-HEMT was utilized for switches Ss1 and Ss2 forming a series bidirectional switch. Experiments were conducted under the following three conditions. Table 7 shows the load parameters at 3.75MHz.

1) **Fixed Inductive Load:**
The series capacitor in the load switcher is manually short-circuited by maintaining Ss1 and Ss2 in the on-state. Therefore, the input impedance of the load network is inductive as $R_{load}+jX_{load}$=55.30+24.98jΩ. The impedance $R_{load}{'}+jX_{load}{'}$ seen from the inverter is also inductive.
2) **Fixed Capacitive Load:**
Ss1 and Ss2 remain off and the series capacitor is not shorted. The series capacitor converts the inductive impedance into capacitive as $R_{load}+jX_{load}$=27.20-35.35jΩ. Therefore, $R_{load}{'}+jX_{load}{'}$ is also capacitive.
3) **Load Fluctuation:**
The load impedance is rapidly transitioned from inductive 55.30+24.98jΩ to capacitive 27.20-35.35jΩ by operating the load-switcher. This operation simulates the suddenly changing load plasma that causes load fluctuations in the plasma system. Ss1 and Ss2 are turned to the off-state from the on-state manually while the inverter is working. This allows the evaluation of the transient response of the inverter soft-switching control under the load changing.

TABLE VII
PARAMETERS OF EXPERIMENTAL LOAD AT 3.75MHZ

Parameter	Symbol	Inductive load	Capacitive load
Equiv. load resistance (Ω)	R_{load}	55.30	27.20
Equiv. load reactance (Ω)	X_{load}	24.98	-35.35
Reflection coefficient in 50Ω system	$\Gamma=\lvert\rho\rvert$	0.236	0.495
Real part of complex reflection coefficient	Re[ρ]	0.101	-0.071
Imaginary part of complex reflection coefficient	Im[ρ]	0.213	-0.490
Phase angle of complex reflection coefficient (deg)	θ_ρ	64.67	-98.21

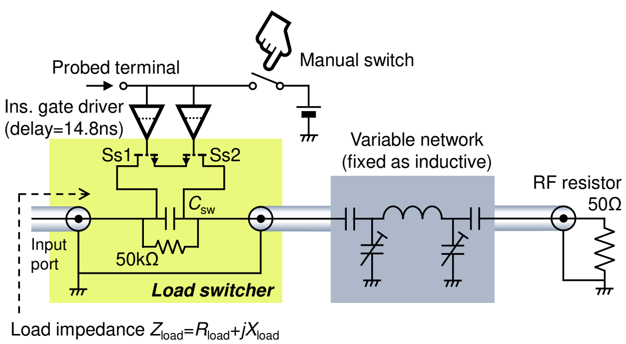

FIGURE 14. Schematic diagram of the experimental dummy load including the manual inductive / capacitive switcher.

VII. EXPERIMENTAL RESULTS

The steady-state waveforms under the fixed loads and the transient response waveforms under load variation were obtained. From the following results, it was confirmed that the inductive and capacitive loads were detected by the proposed observer, the auxiliary switched-inductor was appropriately phase-shifted controlled, and the soft-switching operation was realized in the inverter by the control.

A. EXPERIMENT UNDER FIXED LOAD

The inverter currents were probed by a SS-281A Rogowski probe with 13ns de-skewed, and the waveforms were measured with a HDO4034A oscilloscope. The results for each load condition are as follows.

1) FIXED INDUCTIVE LOAD:

Table 8 shows a comparison of the theoretical values and the system-estimated results of the load condition. t_ρ in Table 8 denotes the phase difference in time domain and is a converted value of θ_ρ. As shown in Table 8, the observed values of t_ρ and θ_ρ have errors of +5.61ns and +7.57°, respectively, compared with the theoretical values. This error is larger than the FPGA phase error of 3.7° in the phase difference detection circuit described in Section 5. Therefore, it is presumed that the error was increased by the voltage-peak-timing detector of the phase difference detection circuit.

Although a slight phase error occurred in the prototype, the proposed observer successfully identified θ_ρ as a positive value, achieving accurate detection of the inductive load.

In the inverter circuit, the input DC voltage, current, and power were 60V, 2.5A, and 150W, respectively. Fig. 15 shows the waveforms of the auxiliary inductor current i_{aux}, the gate-source voltage v_{GS2}, and the drain-source voltage v_{DS2} of the switch S2.

In this load condition, the proposed observer detected the inductive load as designed, and both auxiliary switches Saux1 and Saux2 were kept off properly by the controller. Small i_{aux} seen in Fig. 15 is a negligible leakage current bypassed through the parasitic capacitance of Saux1and Saux2.

TABLE VIII
RESULT OF THE INDUCTIVE LOAD ESTIMATION

Parameter	Symbol	Theoretical value	Estimation result
Reflection coefficient	Γ	0.236	0.24
Reflection phase difference (ns)	t_ρ	47.9	53.51
Reflection phase angle (deg)	θ_ρ	64.67	72.24

Inductive load condition: $R_{load}+jX_{load}$=55.30+24.98j (Ω)

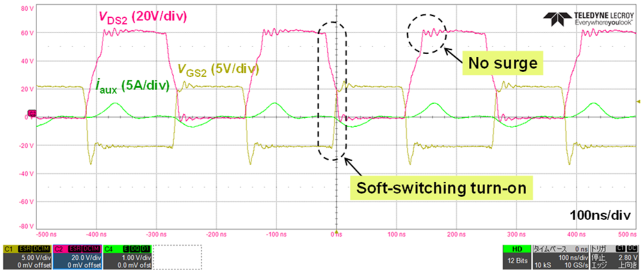

FIGURE 15. Waveforms at inductive load; green wave is Aux. inductor current flowing through parasitic capacitance of Aux. switches.

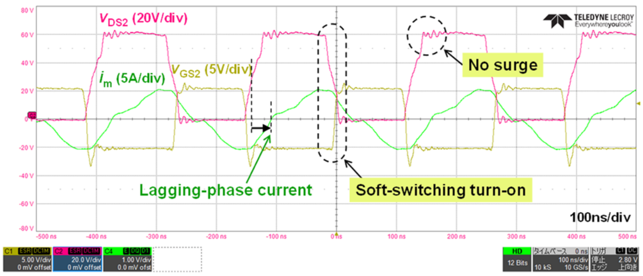

FIGURE 16. Waveforms at inductive load; green wave is output current from the main full-bridge.

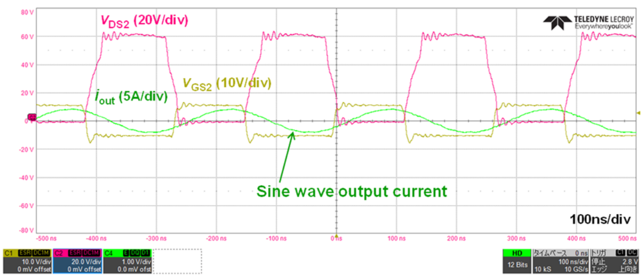

FIGURE 17. Waveforms at inductive load; green wave is output current from the LPF.

Fig. 16 shows the main full-bridge circuit current i_m, the gate-source voltage v_{GS2} of S2, and the drain-source voltage v_{DS2} of S2. As shown in Fig. 16, i_m lags behind v_{DS2}, and no voltage surge is seen on v_{DS2}. These results mean that soft-switching was established due to the inductive load. The small distortion of i_m is caused by a mere leakage current which flows through parasitic capacitances of Saux1 and Saux2.

Fig. 17 shows the sinusoidal output current i_{out}. Amplitude of i_{out} is lower than i_m due to the step-up transformer. i_{out} has almost no distortions due to the series resonator and the LPF. Since the LPF introduces a phase lag of approximately 180° at 3.75MHz, i_{out} lags behind i_m by approximately half a cycle.

2) FIXED CAPACITIVE LOAD WITH NO CONTROL:

This experiment was conducted under the capacitive load condition, with the proposed observer and control deactivated. Only full-bridge switches S1–S4 were operated, and the Saux1 and Saux2 were kept off as completely uncontrolled state. The input DC voltage, current, and power of the inverter were 60V, 2.17A, and 130.2W, respectively.

As shown in Fig. 18, large voltage surges occurred on v_{DS2}, and the phase of i_m advanced relative to v_{DS2}. These results indicate that hard-switching occurred in the full-bridge switch.

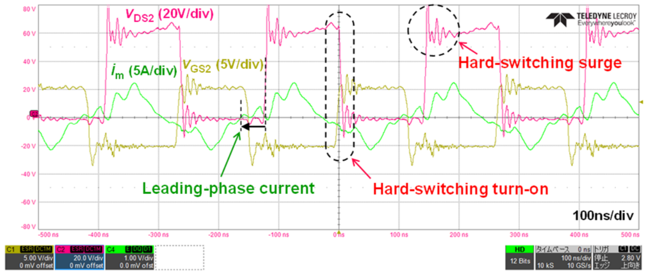

FIGURE 18. Waveforms at capacitive load without control; Hard-switching is occurred. Green wave is output current from main full-bridge.

3) CONTROL UNDER FIXED CAPACITIVE LOAD:

The proposed observer and control circuit were activated in this experiment. The indicator LED shown in Fig. 10 of the phase deference detection circuit lighted, and gate signals for driving Saux1 and Saux2 were generated; it was confirmed that the proposed observer detects the capacitive load. t_{shift} and t_α became 106.4ns and 12.0ns, respectively. These are close to theoretical values 107.99ns and 10.36ns in Tables 6 and 5 for the applicable reflection range of Γ=0.5 and θ_ρ=-90°.

Table 9 shows a comparison of the theoretical values and the system-estimated results of the load condition. The observed values of t_ρ and θ_ρ have errors of +5.2ns and +7.02°, respectively, compared to the theoretical values. As in the inductive load experiment, this error is estimated to be due to the voltage-peak-timing detector in the phase difference detection circuit.

Although a slight phase error occurred in the prototype, the proposed observer successfully identified θ_ρ as a negative value, achieving accurate detection of the capacitive load.

The input DC voltage, current, and power of the inverter were 60V, 1.19A, and 71.4W, respectively. Fig. 19 shows the measured waveforms of v_{GS2}, v_{DS2}, and i_{aux}. i_{aux} is flowing through the auxiliary circuit as a triangular wave. This means that the switched-inductor is functioning by control, and Saux1 and Saux2 conduct current as explained in Fig. 13.

TABLE IX
RESULT OF THE CAPACITIVE LOAD ESTIMATION

Parameter	Symbol	Theoretical value	Estimation result
Reflection coefficient	Γ	0.495	0.5
Reflection phase difference (ns)	t_ρ	-72.75	-67.55
Reflection phase angle (deg)	θ_ρ	-98.21	-91.19

Capacitive load condition: $R_{load}+jX_{load}$=27.20-35.35j (Ω)

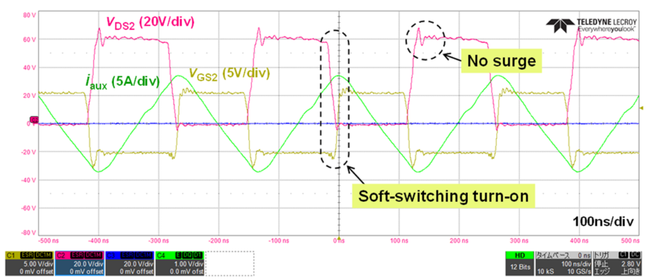

FIGURE 19. Waveforms at capacitive load under controlled; green wave is Aux. inductor current.

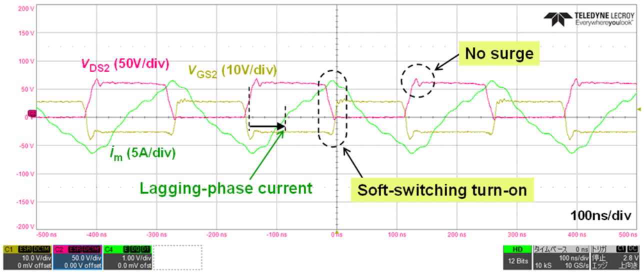

FIGURE 20. Waveforms at capacitive load under controlled; soft-switching operations are achieved. Green wave is output current from the main full-bridge.

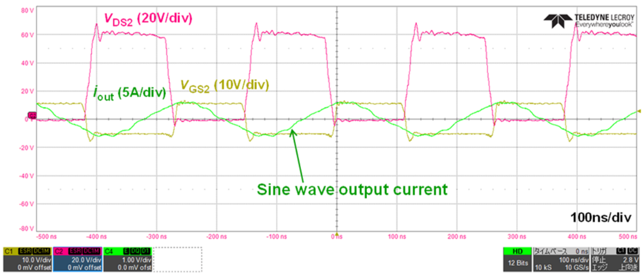

FIGURE 21. Waveforms at capacitive load under controlled; green wave is output current from the LPF.

In addition, i_m lags behind v_{DS2}, and no voltage surge is seen on v_{DS2} as shown in Fig. 20, unlike the case of Fig. 18. It is obvious that the proposed observer and controller provided soft-switching control under the capacitive load condition. Due to the LPF, the waveform of i_{out} in Fig. 21 has less distortion than i_m in Fig. 20 and is closer to a clear sine wave.

B. EXPERIMENT UNDER FLUCTUATING LOAD

The transient response of the proposed system with respect to load fluctuation was measured in this experiment. The oscilloscope was set to be triggered on the turn-off signal of the manual load switcher. The authors measured the delay from the load change to the start of control signal generation and the delay until the inverter operation changes.

1) RESPONSE OF CONTROLLER:

Fig. 22 shows the measured responses of the phase difference detection circuit and the microprocessor. The load impedance is changed from inductive to capacitive by manually turning off the load switcher at '0μs' in Fig. 22. The yellow signal is the on/off state of the load switcher, the magenta signal is the 'capacitive-detection' signal from the phase difference detection circuit, and the blue signal is the 'calculation-completed' signal from the microprocessor at the completion of the calculation of the phase-shift quantity t_{shift}.

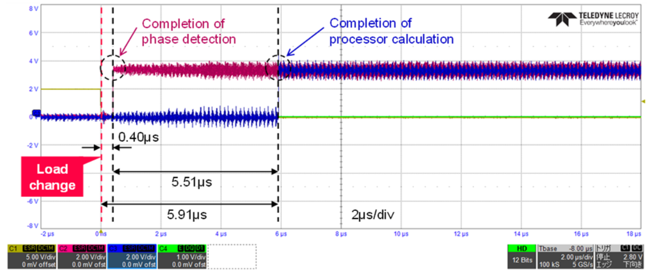

FIGURE 22. Responses in the controller when the load is changed from inductive into capacitive.

As shown in Fig. 22, the phase difference detection circuit detects the phase change of the reflected wave only 0.40μs after the load change. The calculation on the microprocessor takes 5.51μs. The delay due to the microprocessor accounts for 93% of the total delay 5.91μs.

2) RESPONSE OF INVERTER:

Fig. 23 shows the result of transient responses of v_{DS2} and controlled i_{aux}. The load impedance was switched from inductive to capacitive at '0μs'. The yellow signal corresponds to the on/off state of the load switcher, the magenta rectangular waveform is auxiliary phase shifted signal for driving Saux1, the blue waveform is v_{DS2}, and the green waveform is i_{aux}.

As can be seen in Fig. 23, after the load impedance transitioned to capacitive, voltage surges temporarily occurred on v_{DS2}. This temporary hard-switching persisted for only 2.31μs. After that, the microprocessor began to generate the auxiliary drive signal. When this signal started, the amplitude of i_{aux} increased, and hard-switching immediately transitioned to controlled surge-free soft-switching. The response delay of 2.31μs is sufficiently short, allowing only 8 cycles of hard-switching pulses to occur before transitioning to soft-switching.

Incidentally, in Fig. 23, the amplitude of i_{aux} slightly decreases after a 2.27μs time lag from the start of operation of

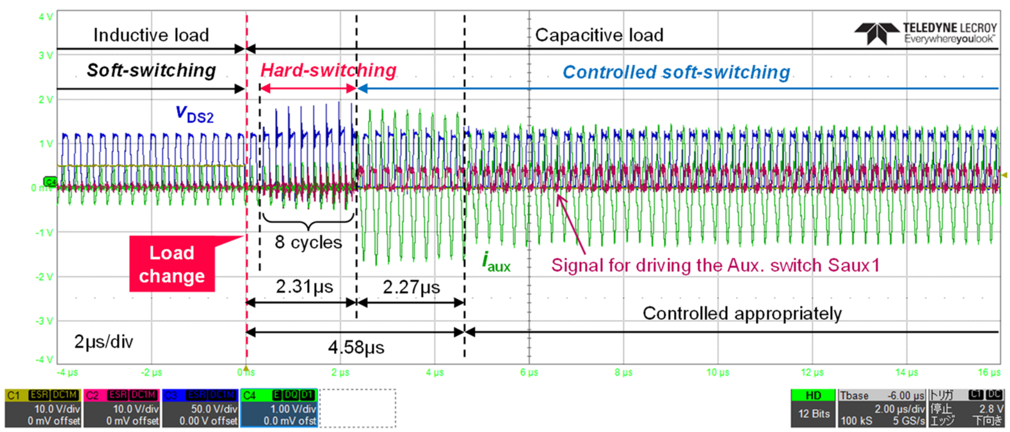

FIGURE 23. Transient waveforms of the inverter when the load is changed from inductive into capacitive.

the auxiliary switch. This is the behavior as programmed. Because the t_{shift} calculation speed of the microprocessor is not sufficiently fast, the authors programed the microprocessor to start Saux1 and Saux2 first with t_α=T_{sw}/4 without waiting for the t_{shift} calculation to complete. Therefore, during the 2.27μs period of t_α=T_{sw}/4, i_{aux} is temporarily larger than necessary.

When 2.27μs had passed and the t_{shift} calculation based on the estimated load condition was completed, t_α was corrected to the appropriate smaller value by phase-shifting with t_{shift}. By this operation, the amplitude of i_{aux} was reduced to an appropriate minimum required amperage.

VIII. CONCLUSION

This study proposed a load estimation method for controlling a MHz resonant inverter. The proposed observer observes traveling and reflected waves instead of voltage and current. In the prototype 3.75MHz inverter system, the control to maintain the soft-switching operation was tested using the proposed observer.

The dynamic and fast control of the inverter system was also achieved by the proposed observer. The hard-switching transitioned to soft-switching in only 8 cycles. Experiments have confirmed that the proposed system detects the capacitive load and prevents continuous hard-switching of the GaN-HEMT switches.

REFERENCES

[1] H. Fujita, H. Akagi, and S. Shinohara, "A 2-MHz 6-kVA voltage-source inverter using low-profile MOSFET modules for low-temperature plasma generators," *IEEE Trans. Power Electron.*, vol. 14, no. 6, pp. 1014–1020, Nov. 1999, doi: 10.1109/63.803394.

[2] R. Peña-Eguiluz, J. Pérez-Martínez, R. López-Callejas, A. Mercado-Cabrera, J. Solís-Pacheco, B. Aguilar-Uscanga, A. Muñoz-Castro, R. Valencia-Alvarado, S. Barocio-Delgado, B. Rodríguez-Méndez, and A. Piedad-Beneitez, "Analysis and application of a parallel E-class amplifier as RF plasma source," *IEEE Trans. Plasma Sci.*, vol. 38, no. 10, pp. 2840–2847, Oct. 2010, doi: 10.1109/TPS.2010.2059048.

[3] J. Choi, Y. Ooue, N. Furukawa, and J. Rivas, "Designing a 40.68 MHz power-combining resonant inverter with eGaN FETs for plasma generation," in *Proc. IEEE Energy Conversion Cong. Expo.*, pp. 1322–1327, Sept. 2018, doi: 10.1109/ECCE.2018.8557680.

[4] S. Park, Y. Sohn, and G. Cho, "SiC-based 4-MHz 10-kW ZVS inverter with fast resonance frequency tracking control for high-density plasma generators," *IEEE Trans. Power Electron.*, vol. 35, no. 3, pp. 3266–3275, Mar. 2020, doi: 10.1109/TPEL.2019.2932056.

[5] M. Yang, E.A. Stolt, Z. Ye, and J.M. Rivas-Davila, "Piezoelectric based class-E resonant inverter for driving surface dielectric barrier discharge plasma," in *Proc. IEEE 10th Int. Power Electron. Motion Control Conf.*, pp. 367–372, May 2024, doi: 10.1109/IPEMC-ECCEAsia60879.2024.10567170.

[6] C. Yong-Nong and K. Chih-Ming, "Design of plasma generator driven by high-frequency high-voltage power supply," *J. App. Res. Technol.*, vol. 11, no. 2, pp. 225–234, Apr. 2013, doi: 10.1016/S1665-6423(13)71532-3.

[7] G. Canal, H. Luna, L. Ruchko, and R. Galvão, "Design and characterization of an RF plasma cleaner," *Braz. J. Phys.*, vol. 40, no. 1, pp. 108–114, Mar. 2010, doi: 10.1590/S0103-97332010000100015.

[8] S. Kumar, B. Kadia, R Singh, A Varia, Y. Srinivas, and S. Kulkarni, "Design aspects of 13.56MHz, 1kW, CW-RF oscillator for plasma production," *J. Phys. Conf. Ser.*, vol. 208, no. 1, pp. 1–4, Mar. 2010, doi: 10.1088/1742-6596/208/1/012012.

[9] Suprabha, M. Pande, K. Dixit, J. Diwan, and C. Kaushik, "Design of 50 kW, 5 MHz RF plasma power supply for low and intermediate level radioactive waste management," in *Proc. IEEE 1st Int. Conf. Power Electron., Intelligent Control Energy Sys.*, pp. 1–3, July 2016, doi: 10.1109/ICPEICES.2016.7853274.

[10] S. El-Hamamsy, "Design of high-efficiency RF Class-D power amplifier," *IEEE Trans. Power Electron.*, vol. 9, no. 3, pp. 297–308, May 1994, doi: 10.1109/63.311263.

[11] J. Rivas, Y. Han, O. Leitermann, A. Sagneri, and D. Perreault, "A high-frequency resonant inverter topology with low-voltage stress," *IEEE Trans. Power Electron.*, vol. 23, no. 4, pp. 1759–1771, July 2008, doi: 10.1109/TPEL.2008.924616.

[12] F. Raab, "GaN-FET Class-E amplifier for 60-MHz radar," in *Proc. IEEE 50th Eur. Microw. Conf.*, pp. 1099–1102, Jan. 2021, doi: 10.23919/EuMC48046.2021.9338069.

[13] A. Oyane, T. Senanayake, M. Masuda, J. Imaoka, and M. Yamamoto, "13.56MHz half-bridge GaN-HEMT resonant inverter achieving high power, low distortion, and high efficiency by 'L-S Network'," *IEICE Trans. Electron.*, vol. E105.C, no. 9, pp. 407–418, Sept. 2022, doi: 10.1587/transele.2021ecp5048.

[14] M.T. Tran and W. Choi, "Design and implementation of a constant current and constant voltage wireless charger operating at 6.78 MHz," *IEEE Access*, vol. 7, pp. 184254–184265, Dec. 2019, doi: 10.1109/ACCESS.2019.2959981.

[15] K. Leou, G. Chen, C. Lin, T. Lin, and C. Tsai, "Measurement of time varying RF impedance of a pulsed inductively coupled plasma," in *Proc. IEEE Int. Conf. Plasma Sci.*, pp. 275–275, May 2002, doi: 10.1109/PLASMA.2002.1030571.

[16] M. Sobolewski "Current and voltage measurements in the gaseous electronics conference RF reference cell," *J. Res. Natl. Inst. Stand. Technol.*, vol. 100, no. 4, pp. 341–351, July 1995, doi: 10.6028/jres.100.026.

[17] K. Itakura, H. Kakemizu, H. Nakaido, K. Umetani, E. Hiraki, T. Ikenari, and S. Kawano, "Soft-switching technique applicable to capacitive load for resonant inverter of plasma generator," in *Proc. IEEE Annu. Conf. Ind. Electron. Soc.*, pp. 1556–1562, Oct. 2017, doi: 10.1109/IECON.2017.8216264.

[18] K. Itakura, H. Kakemizu, H. Nakaido, K. Umetani, E. Hiraki, T. Ikenari, and S. Kawano, "Experimental evaluation of high-frequency inverter with parallel connected inductor for plasma generator," in *Proc. IEEJ Ind. App. Soc. Conf.*, no. 1–77, pp. 261–266, Aug. 2016 (in Japanese).

[19] S. Ziegler, R.C. Woodward, H.H. Iu, and L.J. Borle, "Current sensing techniques: a review," *IEEE Sensors J.*, vol. 9, no. 4, pp. 354–376, Apr. 2009, doi: 10.1109/JSEN.2009.2013914.

[20] H. Chen and B. Huang, "Integrated G2V/V2G switched reluctance motor drive with sensing only switch-bus current," *IEEE Trans. Power Electron.*, vol. 36, no. 8, pp. 9372–9381, Aug. 2021, doi: 10.1109/TPEL.2021.3054875.

[21] J. Lee, H. Park, J. Lee, and S. Hong, "Understanding of RF impedance matching system using VI-probe," *J. Semi. Disp. Technol.*, vol. 19, no. 3, pp. 43–48, Sept. 2020.

[22] Z. Wang, X. Wei, H. Fang, H. Zhang, and Y. Zhang, "A compact and broadband directional coupler for high-power radio frequency applications," *IEEE Microw. Wireless Compon. Lett.*, vol. 30, no. 2, pp. 164–166, Feb. 2020, doi: 10.1109/LMWC.2020.2964672.

[23] S. Guha, A. Misra, and A. Reza, "Design and development of a broadband RF power meter for RF amplifier," in *Proc. IEEE Appl. Electromagnetics Conf.*, pp. 1–2, Dec. 2017, doi: 10.1109/AEMC.2017.8325757.

[24] A. Oyane, K. Itakura, K. Umetani, E. Hiraki, T. Ikenari, and S. Kawano, "Soft-switching control circuit based on traveling and reflected waves for high-frequency resonant inverter applicable to capacitive load impedance," in *Proc. IEEE Annu. Conf. Ind. Electron. Soc.*, pp. 3051–3056, Oct. 2018, doi: 10.1109/IECON.2018.8592832.

[25] T. Iseki, M. Nakaoka, Y. Okazaki, Y. Nishimori, and S. Oomae, "Zero-voltage soft-switching RF inverter system for plasma generation," *IEICE Tech. Rep.*, vol. 97, no. 542, pp. 17–22, Feb. 1998 (in Japanese).

[26] M. Salem, J. Loiseau, and B. Held, "Impedance matching for optimization of power transfer in a capacitively excited RF plasma reactor," *Eur. Phys. J. App. Phys.*, vol. 3, no. 1, pp. 91-95, July 1998, doi: 10.1051/epjap:1998208.

[27] C.G. Sontheimer and R.E. Fredrick, "Broadband directional coupler," U.S. Patent 3426298, Feb. 1969.

[28] J. Lai, R.W. Young, G.W. Ott, J.W. McKeever, and F.Z. Peng, "A delta-configured auxiliary resonant snubber inverter," *IEEE Trans. Ind. App.*, vol. 32, no. 3, pp. 518–525, May 1996, doi: 10.1109/28.502162.

[29] H. Sugimura, S. Kwon, H. Ogiwara, E. Hiraki, and M. Nakaoka, "A new phase shifted ZVS-PWM controlled full bridge series resonant high frequency inverter with auxiliary active quasi-resonant commutation circuit," in *Proc. IEEE Power Conv. Conf.*, pp. 1505–1511, Apr. 2007, doi: 10.1109/PCCON.2007.373163.

[30] Y. Xia and R. Ayyanar, "Naturally adaptive, low-loss zero-voltage-transition circuit for high-frequency full-bridge inverters with hybrid PWM," *IEEE Trans. Power Electron.*, vol. 33, no. 6, pp. 4916–4933, Jun. 2018, doi: 10.1109/TPEL.2017.2734638.

[31] E. Chu, Z. Chen, H. Xie, and H. Zhang, "Modified double auxiliary resonant commutated pole inverter and its modulation strategy," *IEEE J. Emerg. Sel. Topics Power Electron.*, vol. 8, no. 4, pp. 4467–4481, Dec. 2020, doi: 10.1109/JESTPE.2019.2939168.

AOI OYANE received the M.S. and Ph.D. degrees in engineering from Nagoya University, Nagoya, Japan, in 2020 and 2023, respectively.

He is currently a Project Assistant Professor with The University of Tokyo, Chiba, Japan. His research interests include high-frequency high-power inverters, resonant wireless power transfer systems, and dynamic wireless power transfer for moving electric vehicles.

Dr. Oyane is a member of the Institute of Electrical Engineers of Japan (IEEJ) and the Institute of Electronics, Information and Communication Engineers (IEICE).

KAZUHIRO UMETANI (Member, IEEE) received the M.S. and Ph.D. degrees in geophysical fluid dynamics from Kyoto University, Kyoto, Japan, in 2004 and 2007, respectively, and the second Ph.D. degree in electrical engineering from Shimane University, Matsue, Japan, in 2015.

From 2007 to 2008, he was a Circuit Design Engineer with Toshiba Corporation, Japan. From 2008 to 2014, he was with the Power Electronics Group, Denso Corporation, Japan. From 2014 to 2020, he was an Assistant Professor with Okayama University, Okayama, Japan. From 2020 to 2021, he was an Associate Professor with Tohoku University, Miyagi, Japan. He is currently an Associate Professor with Okayama University, Okayama, Japan. His research interests include new circuit configurations in power electronics and power magnetics for vehicular applications.

Dr. Umetani is a member of the Institute of Electrical Engineers of Japan (IEEJ) and the Japan Institute of Power Electronics

EIJI HIRAKI (Member, IEEE) received the M.S. and Ph.D. degrees from Osaka University, Osaka, Japan, in 1990 and 2004, respectively.

In 1990, he joined Mazda Motor Corporation. From 1995 to 2013, he was with the Power Electronics Laboratory, Yamaguchi University, Yamaguchi, Japan. He is currently a Professor with the Electric Power Conversion System Engineering Laboratory, Okayama University, Okayama, Japan. His research interests include circuits and control systems of power electronics, particularly soft-switching technique for high-frequency switching power conversion systems.

Prof. Hiraki is a Member of the Institute of Electrical Engineers of Japan (IEEJ) and the Japan Institute of Power Electronics.